Applied Water Science (2023) 13:187
https://doi.org/10.1007/s13201-023-01978-3

ORIGINAL ARTICLE

Delineation of Nubian sandstone aquifer using geophysical data around Nuweiba area, Sinai, Egypt

S. A. S. Araffa[1] · H. S. Sabet[2] · M. H. Mahmoud[1]

Received: 20 January 2023 / Accepted: 1 August 2023 / Published online: 31 August 2023

Abstract
The Nubian sandstone aquifer (NSA) is defined by using 19 vertical electrical sounding (VES) stations, 201 gravity stations, which define the structures that control the configuration of the NSA, and 183 land magnetic stations, which define the lower surface of the NSA by determining the depth of the basement surface. In order to assess the top of the NSA, we collected and analyzed 19 deep VESes. The upper surface depth of the NSA spans from 707 to 1154 m, according to the interpretation results for various geophysical data. Additionally, the aquifer's resistivities ranged from 30.2 to 477 Ω m, which indicates good groundwater quality. According to the interpretation of the gravity result, the study region is influenced by many structural characteristics of different trends, including northwest–southeast, northeast–southwest, and east–west trends. The upper surface depth of crystalline rocks (also known as basement rocks) is determined by three-dimensional magnetic modeling to range between 967 and 4122 m.

Keywords Geophysical tools · Gravity · Magnetic · Groundwater aquifers · VES · Fault elements

Introduction

The Sinai Peninsula is a significant part of Egypt, having an area of ~62,000 km^2. It lies toward the east of Northern Egypt and is bounded by the Suez Gulf, Aqaba Gulf, Mediterranean Sea, and the Red Sea (Fig. 1). In Sinai, most areas experience water scarcity, particularly in central Sinai. Nubian sandstone aquifer (NSA) is the principal aquifer in the region. It is part of the Nubian sandstone aquifer system (NSAS), which is considered one of the most significant and potable groundwater basins in the world. It extends over a vast area in Egypt, Libya, Sudan, and Chad in NE Africa and bears its largest fossil water reservoir. The Nubian sandstone formation ranges from Cambrian to Upper Cretaceous and overlies a Precambrian basement composed of sandstones intercalated with some clays. The water sources that recharge the Nubian sandstone aquifer (NSA) in Sinai are rainfalls and flash floods at high altitudes in the mountains in the south of Sinai, with regions with high topography and characterized by densely populated areas rain throughout most days of the year. The rainfall distribution varies spatially across the area, hence affecting the groundwater recharge within the area (Shebl et al 2022; Araffa et al 2022; El-Badrawy et al. 2021). For exploring groundwater potentiality, geophysical methods such as geoelectric, magnetic, and gravity are important (Telford et al. 1995; Zohdy et al. 1974; Nabighian and Macnae 1991). The area under investigation is bounded by 28° 46′ and 29° 41′ N and 33° 51′ and 34° 41′ E and represents an area of 3900 km^2. This study assesses the NSA in the investigated area. It aims to delineate the tectonic features and structures, which are essential in the distribution and configuration of aquifers in the investigated area.

Moreover, in addition to the thickness of NSA, it defines the depth of the top of crystalline rocks. The area under investigation has been the subject of numerous geophysical applications. (Sultan et al. 2009) integrated geophysical investigation in northwestern Sinai to specify the subsurface structures and assess water occurrences. Araffa et al.

✉ S. A. S. Araffa
sultan_awad@yahoo.com

H. S. Sabet
hassansalehsabet@yahoo.com

M. H. Mahmoud
mohamed.hussien992@yahoo.com

[1] National Research Institute of Astronomy and Geophysics (NRIAG), Cairo, Egypt

[2] Geology Department, Faculty of Science, Al Azhar University, Cairo, Egypt

2015 used different geophysical techniques to delineate groundwater occurrences in central Sinai, where they concluded that the depth of NSA is within 978–1074 m. Ibrahim et al. 2004 applied electric resistivity measurements to the quaternary water-bearing zone in northwestern Sinai. Santos et al. 2006 used the joint inversion of gravity data and DC electric resistivity to delineate the Quaternary aquifer in northwest Sinai. El-Badrawy et al. 2021 employed multipotential methods for delineating underground water aquifers in central Sinai. Moreover, researchers Rubin et al. 2006; Binley et al. 2015 conducted hydro-geophysical studies to improve understanding of subsurface processes over

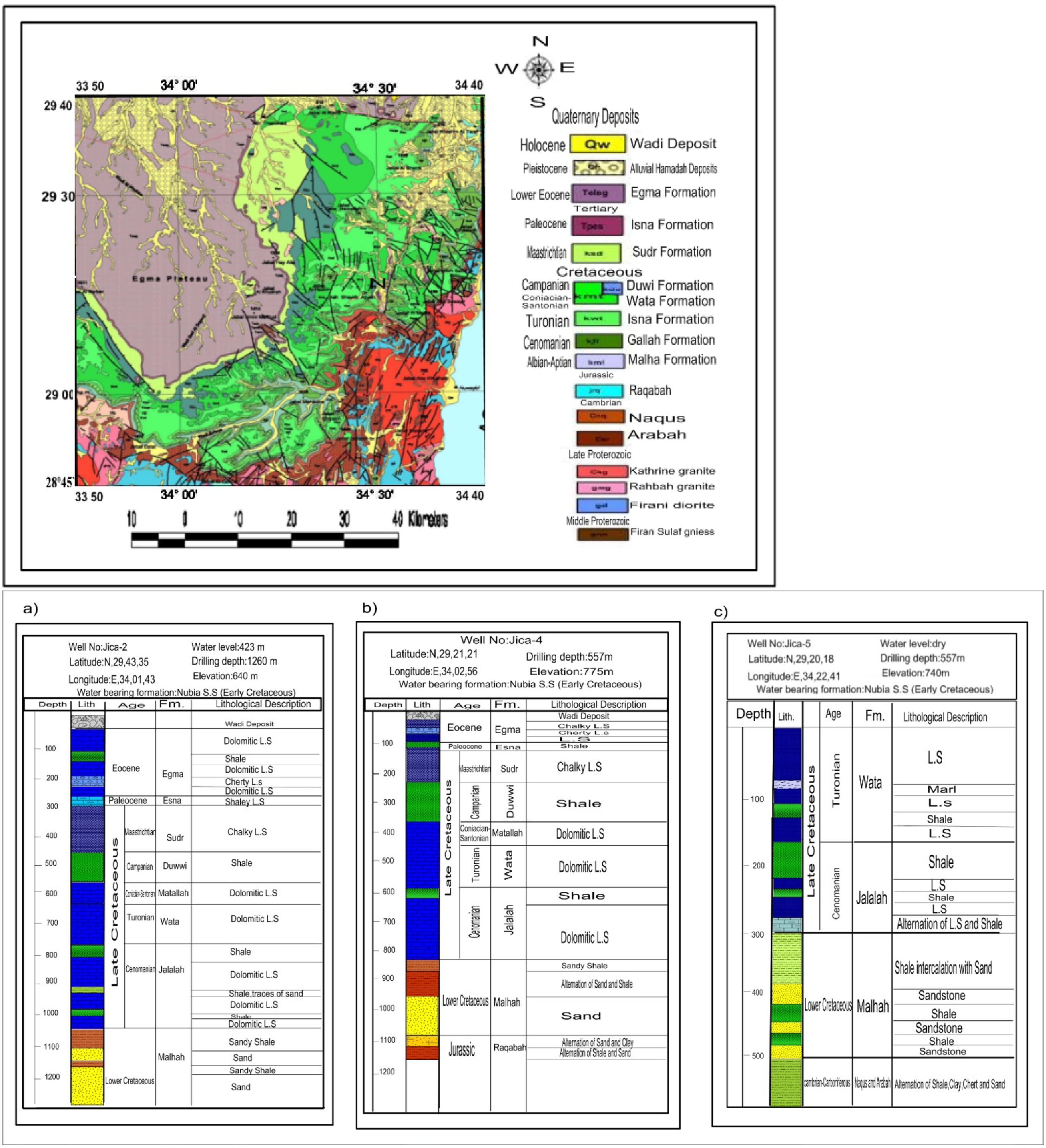

Fig. 1 The upper part is the geological map of the studied area (modified after UNSECO Cairo Office 2005). The lower part is the lithostratigraphic sequence of JICA Well No. 2, JICA Well No 4, and JICA Well No 5 (after JICA 1992)

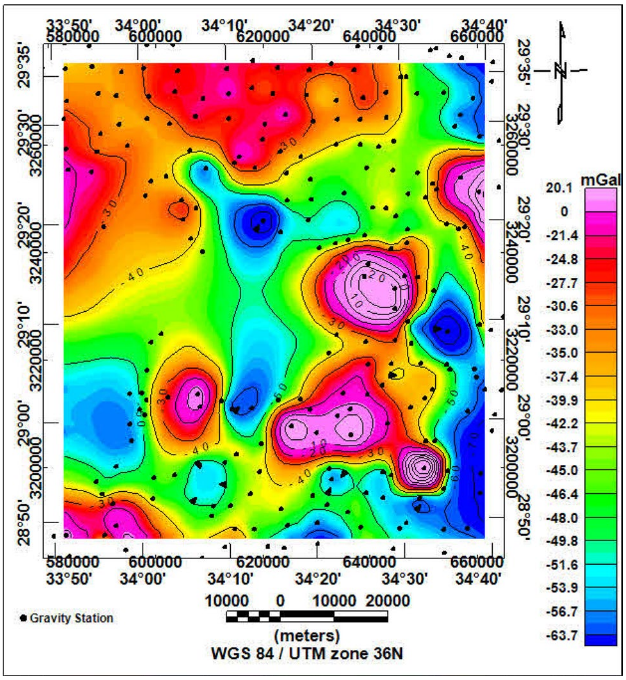

Fig. 2 Bouguer anomaly map of the studied area. The dots of black color represent the locations of measured stations

Table 1 Correlation factor for different orders

Order (r)	Value
1–2	0.860605741
2–3	0.538554068
3–4	0.047894331
4–5	0.994505044

multiple scales; Parsekian et al. 2015 employed multiscale geophysical imaging in important zones; Linde and Doetsch et al. 2016 examined the joint inversion in near-surface geophysics and hydro-geophysics. The hydraulic parameters of the subsurface layer were estimated using the double hydro-geophysical inversion of time-lapse surface GPR data. Busch et al. 2013; Camporese et al. 2012 used electrical resistivity tomography monitoring to assess local hydraulics. Dlubac et al. 2013 used nuclear magnetic resonance (NMR) logging to analyze hydraulic conductivity in the top plainsman aquifer in Nebraska, USA. Feng et al 2013 estimated the scarcity of underground water in northern China using climate experiment data, gravity recovery, and ground-based measurements. Araffa 2013 investigated northeastern Greater Cairo using geoelectrical, gravity, and magnetic tools to delineate subsurface structures and groundwater occurrences. Elbarbary et al. 2021 performed geophysical studies for groundwater exploration at northern Sinai. Other researchers conducted hydro-geophysical investigations (Irving and Singha 2010; Hinnell et al. 2010; Pollock and Cirpka 2012; Van Dam, 2014; Gian, 2003). Furthermore, geoelectric tools have been employed for geotechnical studies (Araffa 2010; Sultan and Santos 2008; Mohamed et al 2012; Al Deep et al. 2021; Abdel Zaher et al. 2018).

Geologic setting

The Sinai Peninsula is characterized by different topographic features where high mountains occupy the southern part; these high mountains have the height of the highest peak that reaches 2750 meters. The Nubian sandstone aquifer (NSA) of the Lower Cretaceous in the Sinai Peninsula extends the sandstone formation of the African shield. In the central and southern Sinai, the aquifer is composed of alternating beds of sandstone and shale, and north of the folded zone of the El-Maghara-El-Halal Mountains, the facies changes to carbonate and shale. Low lands characterize the northern Sinai; most Wadis are in the southerly to a northerly direction. The investigation area is covered by various rocks that belong to different formations of different ages. The geological setting of the examined region is represented by the surface geological map, which is developed by UNESCO Cairo Office (2005) (Fig. 1); this map shows that most geological units belong to different geological ages. The subsurface lithostratigraphic succession is obtained from existing boreholes drilled in the examined area by Japan International Cooperation Agency JICA (1992) as in JICA-2, JICA-4, and JICA-5 (Fig. 1). The oldest rocks, which comprise thick-bedded sandstone, belong to the Cambrian age in the examined area. In contrast, the Jurassic rock units of Raqabah FM are composed of sand and sandstone with gravel bands intercalated with shale and outcrops at Wadi Qudayrah. Lower Cretaceous rock units in the investigated area include different formations such as Malhah, Jalalah, Wata, Matallah, Duwwi, and Sudr. These formations comprise sandstones intercalated with shale and represent the target under the groundwater aquifer in NSA (Hassanin 1997). The NSA, which overlooks various rocks of different formations, belongs to the Paleocene–Early Eocene. These rocks are reported in the Esna Shale Formation. Egma Formation belongs to the Pliocene, which comprises gravels of a thickness of ~ 15 m. Quaternary deposits occupy most low land and Wadis. The investigated area is the plurality of intensively faulted regions in Sinai (Said 1962). Faults dissect certain pieces of faulted zones in these trends: E–W, N–S, NE–SW, and NW–SE.

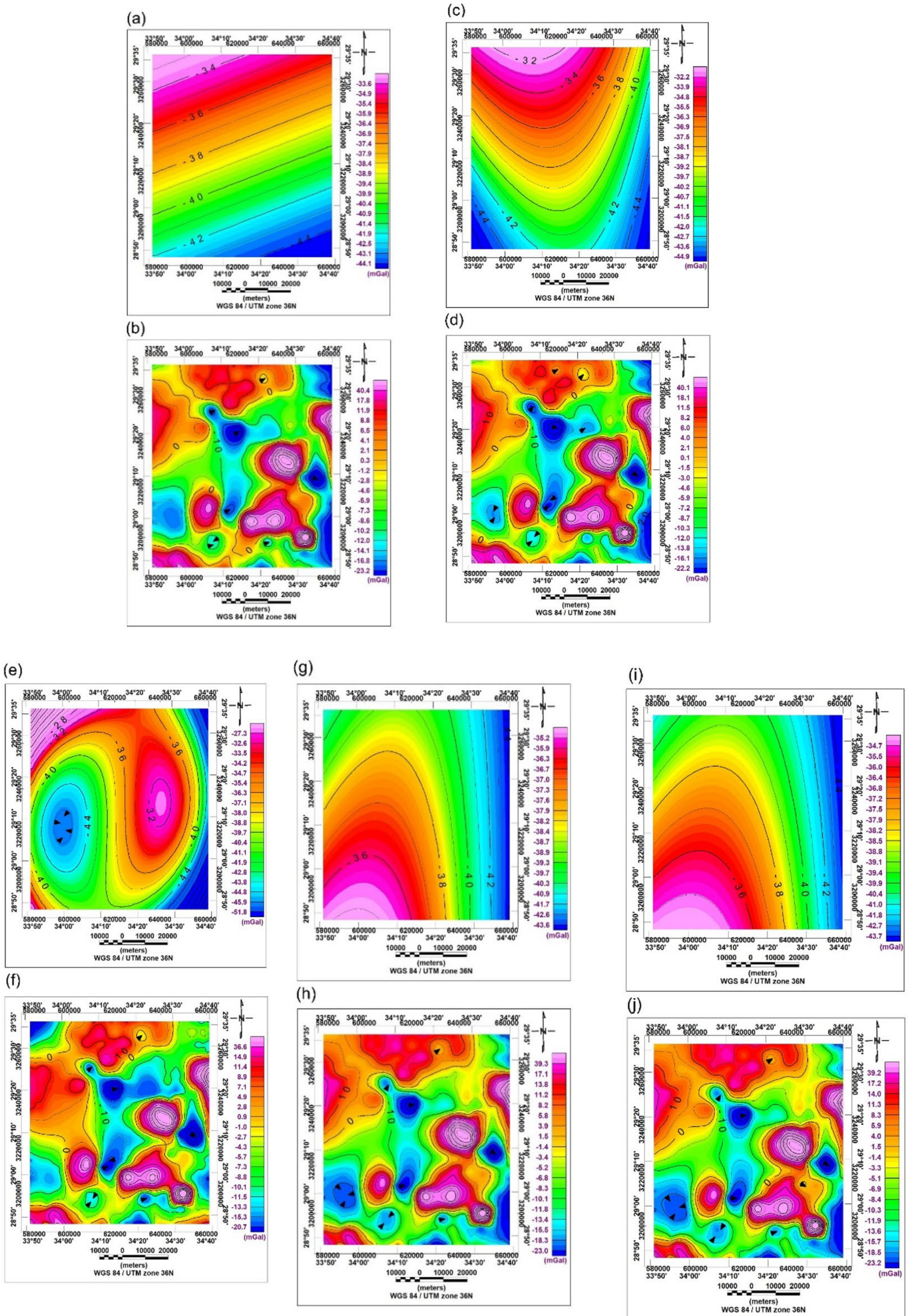

Fig. 3 **a** First-order regional gravity anomaly map. **b** First-order residual gravity anomaly map **c** Second-order regional gravity anomaly map. **d** Second-order residual gravity anomaly map. **e** Third-order regional gravity anomaly map. **f** Third-order residual gravity anomaly map. **g** Fourth-order regional gravity anomaly map. **h** Fourth-order residual gravity anomaly map. **i** Fifth-order regional gravity anomaly map. **j** Fifth-order residual gravity anomaly

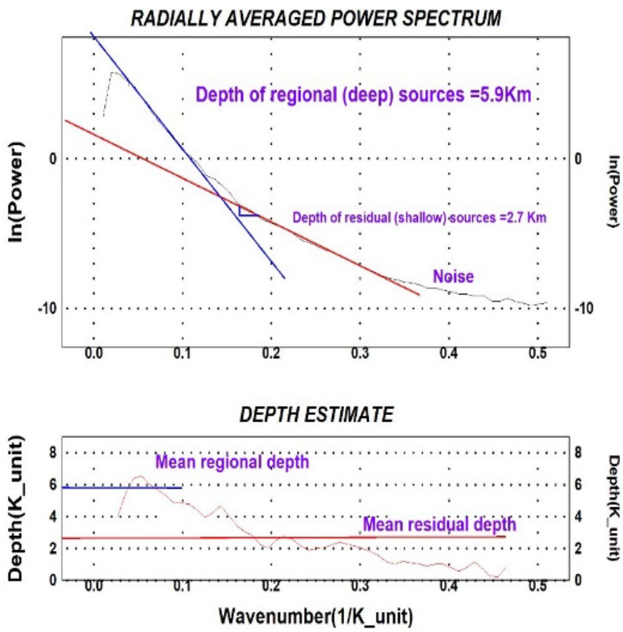

Fig. 4 Power spectrum of gravity data showing the corresponding averaging regional and the residual depth

Geophysical methods

We used three geophysical tools: a geoelectrical tool for delineating the upper surface of NSA; a gravity tool to detect the structural features that have a direct effect on the distribution of NSA; a magnetic tool to estimate the depth of crystalline rocks and delineating the lower surface of the aquifer; and thickness of NSA.

Gravity method

This study uses gravity data for delineating structures that directly impact the groundwater distribution and aquifer geometry. Gravity measurements are obtained using CG-3 Autograv with a sensitivity of 0.01 mGal via 201 gravity stations of space between stations 2 and 3 km apart, distributed based on topography and tracks in the lowlands of the investigated area. The gravity data measurements are reduced for various corrections such as drift, latitude, elevation, tide, and topographic corrections (Oasis Montaj 2015). The final corrected gravity data can be used for developing the gravity anomaly map (Fig. 2), which reflects various anomalies of high gravity (20 mGal) in the northwestern, eastern, southwestern, and central parts. However, the southeastern part and other regions in the southern, northeastern, eastern, and central parts show low gravity anomalies (−71 mGal).

Gravity data filtration

The regional and residual components are separated to filter anomalies from deep-seated and shallow sources. We used the least-squares technique and the high- and low-pass technique for gravity filtration. The least-squares technique was used until the fifth order. Table 1 shows the correlation factor of every two successive orders (r), with the fourth order, referred to as the best (Fig. 3).

Results of gravity interpretation

The interpretation of gravity data started with separating the two components of low- and high-pass components. They are separated through wavenumbers' high- and low-pass technique (0.018 1/km) (Fig. 4). The average depth of deep sources is 5.91 km, whereas the depth of the shallow source is 2.71 km. The residual gravity map for fourth-order and low-pass filter maps (Fig. 5a and b) is used to delineate the study area's structural elements. Also, the Euler technique is used to estimate the different Euler solutions, which are superimposed gravity maps with structural index (SI) = 0 where various sources' depth locations are reported by different color circles, which vary from ~1 to 5 km (Fig. 5e).

Moreover, the Euler deconvolution delineates faults or contact at different depth levels dissecting the examined area. The important trends of structural elements are determined by the fourth-order residual gravity anomaly map, high-pass gravity map, and Euler deconvolution of structural index equal 0. The trends of these fault elements are represented by rose diagrams (Fig. 5a–f). The major trend is northeast–southwest (Aqaba Gulf trend).

Magnetic method

Magnetic data were obtained via 183 magnetic land stations at the same sites of gravity stations using two ENVI-MAG magnetometers of a sensitivity of 1 nT. One of them is used in the field survey, whereas the other is used for base station recording to calculate the diurnal variation (diurnal correction). As per (Oasis Montaj 2015), the magnetic data were corrected for IGRF correction; moreover, after correlations, they are represented by the total intensity magnetic map (Fig. 6a). The total intensity of the magnetic map for corrected magnetic data can be reduced to the pole before applying any interpretation. Thus, magnetic data interpretation begins with RTP (Fig. 6b); the IGRF parameters applied to generate the RTP map were inclination of 43.157°, declination of 3.34°, and field strength of 43,076.2 nT. Previously, Baranov 1957; Baranov 1975; Baranov, and Naudy 1964; Bhattacharyya 1965 explained the RTP procedure. The RTP map was used for magnetic processing and interpretation to determine the depth of the upper surface.

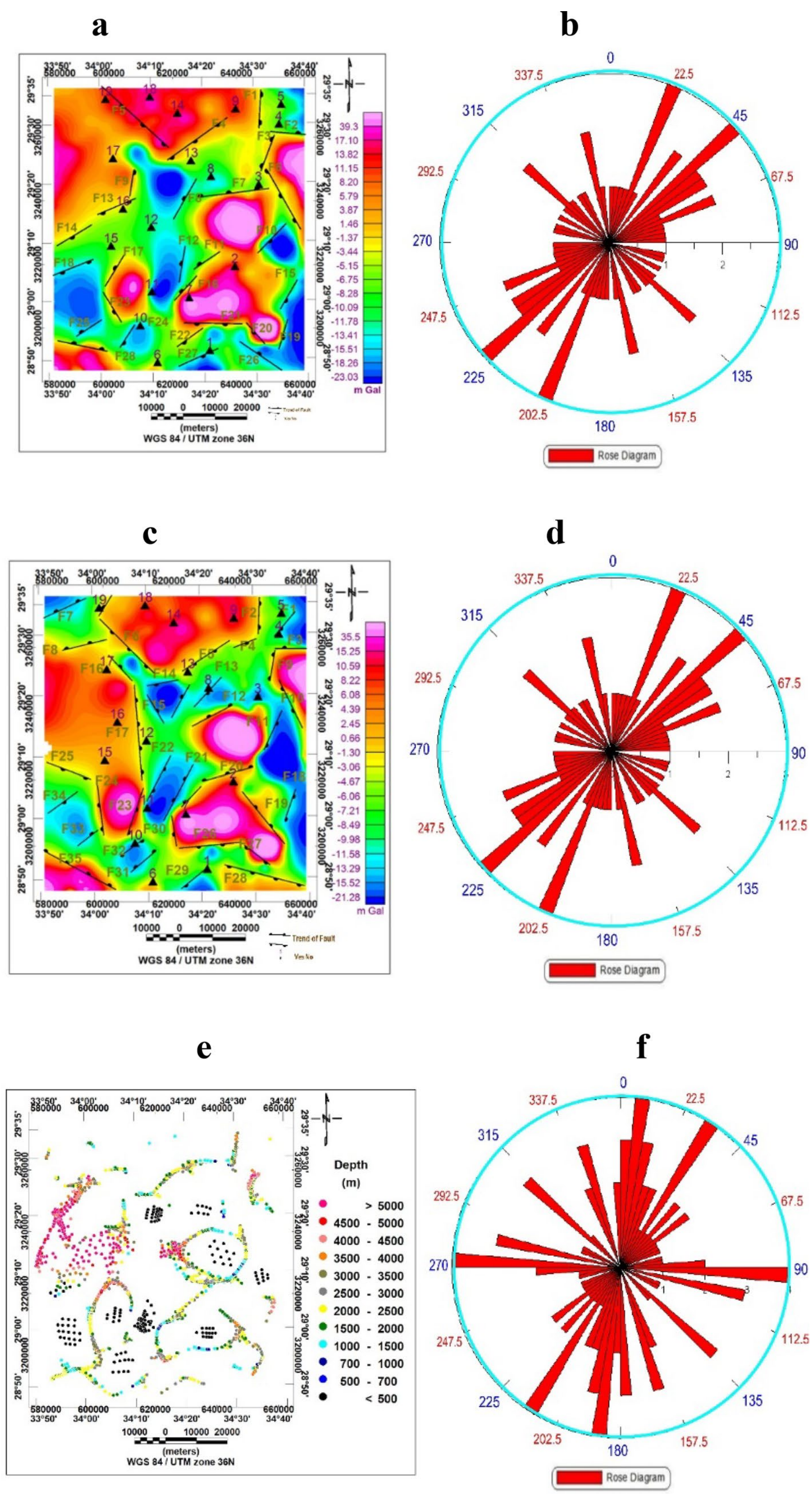

Fig. 5 **a** Fault elements dissecting studied area from residual gravity of fourth order. **b** Rose diagram shows the trends of the fault element from residual gravity of fourth order. **c** Fault elements dissecting studied area from high pass. **d** Rose diagram shows the trends of the fault element from high pass. **e** Euler solutions with the structural index of zero. **f** Rose diagram shows the trends of the fault element from Euler solutions that have a structural index of zero

a

b

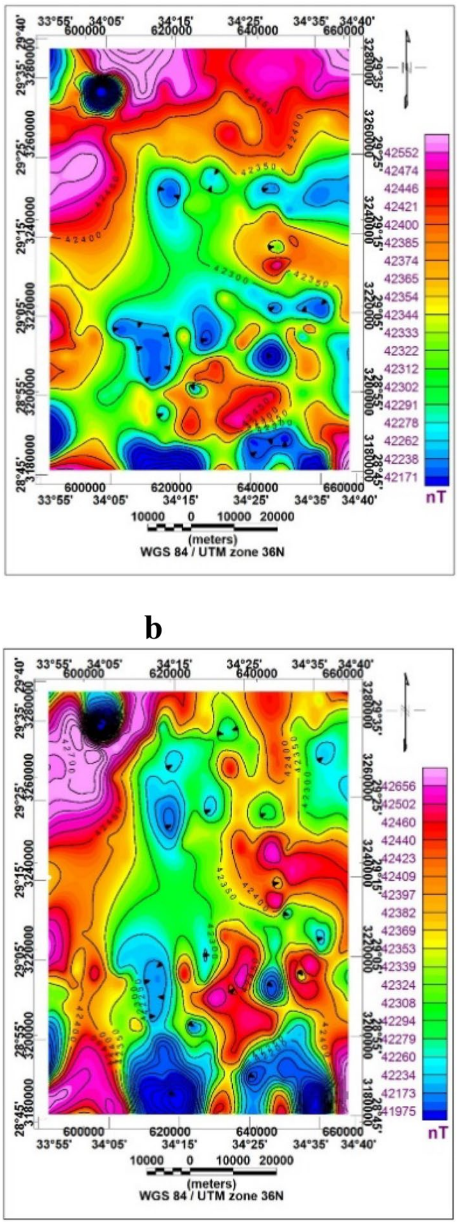

Fig. 6 **a** Total intensity magnetic map. **b** Total intensity magnetic map reduced to the pole

Magnetic interpretation results

3D magnetic modeling The three-dimensional (3D) magnetic modeling is applied to RTP data using GMSYS-3D, which estimates the depth of the crystalline basement rocks and susceptibility of 7850 μCGS. There is a correlation between observed and calculated maps (Fig. 7).

Basement relief map The basement depth map is drawn based on the results of 3D magnetic modeling (Fig. 8), which shows the upper surface of crystalline rocks (basement) and has a value between 967 and 4122 m.

Geoelectric method

Geoelectrical methods are primary tools for groundwater exploration, particularly vertical electrical soundings (VES). The subsurface and water-saturated layers can be precisely defined based on electrical resistivity. The penetration depth for electrical current is directly proportional to the distance between current electrodes (AB); the electrical resistivity data are acquired and represented by 19 VESes (Fig. 9a). The data acquired through the Schlumberger array of AB/2 vary from 5 to 3000 m using certain devices produced by IRIS (Syscal-R2 instrument). The Syscal-R2 instrument is combined with a 1200 W AC/DC converter. The collected geoelectrical data are arranged to cover the investigated area along southwest–northeast and west–east trending lines as per topographic features. Certain VES stations, such as VES4, VES8, and VES19, are acquired besides drilled boreholes JICA-4, JICA-5, and JICA-2, respectively, for correlation between the results of geoelectrical and borehole data. The quantitative interpretation of resistivity data was used via a manual method that used two-layer master curves (Koefoed 1960). The manual interpretation of results was used as a preliminary model for IPI2WIN-1D 2000 (Bobachev et al. 2001) to estimate true resistivities and depths for the curve of each VES (Fig. 9b). The interpretation consequences for geoelectrical data show that most results of VES stations comprise six to nine geoelectric units of different thicknesses.

Results of geoelectrical data

Geoelectrical cross sections Five geoelectric cross sections are obtained from the final quantitative interpretation of VES stations along with five profiles: A–A′, B–B′, C–C′, D–D′, and E–E′ (Fig. 10). These geoelectrical cross sections show the six geoelectrical units of different lithological compositions. The first geoelectric unit comprises multiple rock fragments representing alluvial deposits with varying thicknesses, ranging from 0.7 to 202.6 m, and resistivity values ranging from 7 to 980 Ω m of the Quaternary age. The second geoelectrical unit belongs to the Upper Cretaceous age and comprises limestone of various thicknesses between 13.8 and 259 m; the differentiating resistivity is between 20.2 and 1196 Ω m. The third geoelectrical unit includes a sandstone unit that belongs to the rocks of the Upper Cretaceous with thicknesses ranging from 34.1 to 372 m and resistivities between 8.6 and 848 Ω m. The fourth geoelectrical unit comprises limestone and dolomitic limestone, reflecting the number of resistivity values ranging from 28.5 to 1971 Ω m, as well as thickness values between 116 and 459 m.

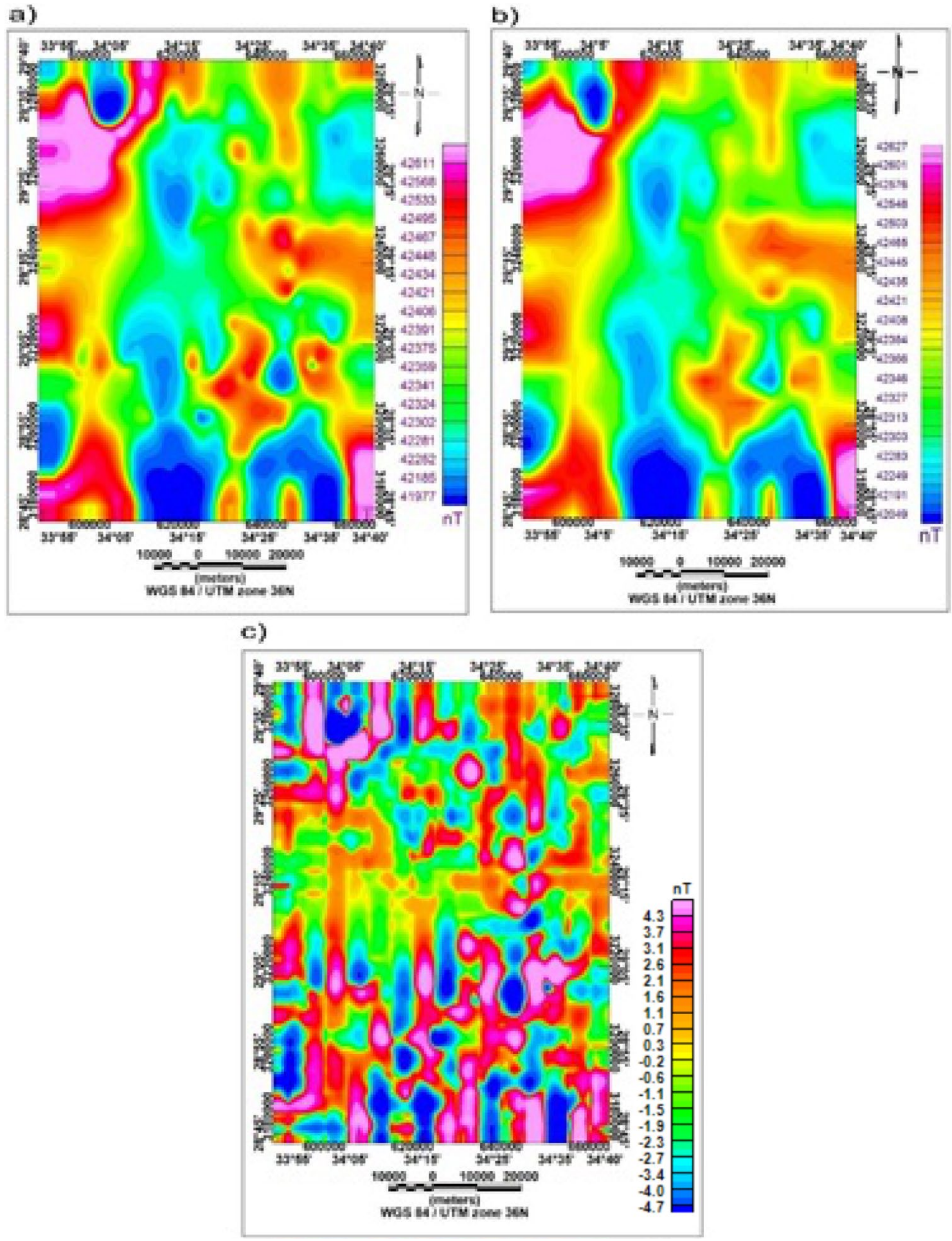

Fig. 7 Outputs of GMSYS-3D modeling: **a** observed magnetic anomalies; **b** calculated magnetic anomalies; **c** error percentage ranged from 0.1 to 1

The fifth geoelectrical unit comprises limestone, dolomite limestone, marls, and shales of the Upper Cretaceous with various resistivity values ranging from 1.98 to 223 Ω m, and the thickness values are between 142 and 397 m. The sixth geological unit represents NSA in the examined area. The depth at the top of this unit is between 707 and 1154 m, which comprises thick-bedded grained sandstones. The age of this unit (aquifer) is the Lower Cretaceous and has resistivities ranging from 30.2 to 477 Ω m, which exhibits low salinity water in the investigated area.

Depth map to the top of NSA (sixth geological unit) The interpretation of VES data for developing the depth to the top of NSA reflected the low values of depths at the southeastern part of the investigated area (654–700 m); however, the depth was ~ 1300 m in the western part (Fig. 11a).

Isoresistivity Map of NSA (sixth geological unit) The true resistivity values of quantitative VES data interpretation are obtained, and northern parts of the investigated area have high resistivity values of ~ 350–477 Ω m. In contrast, the

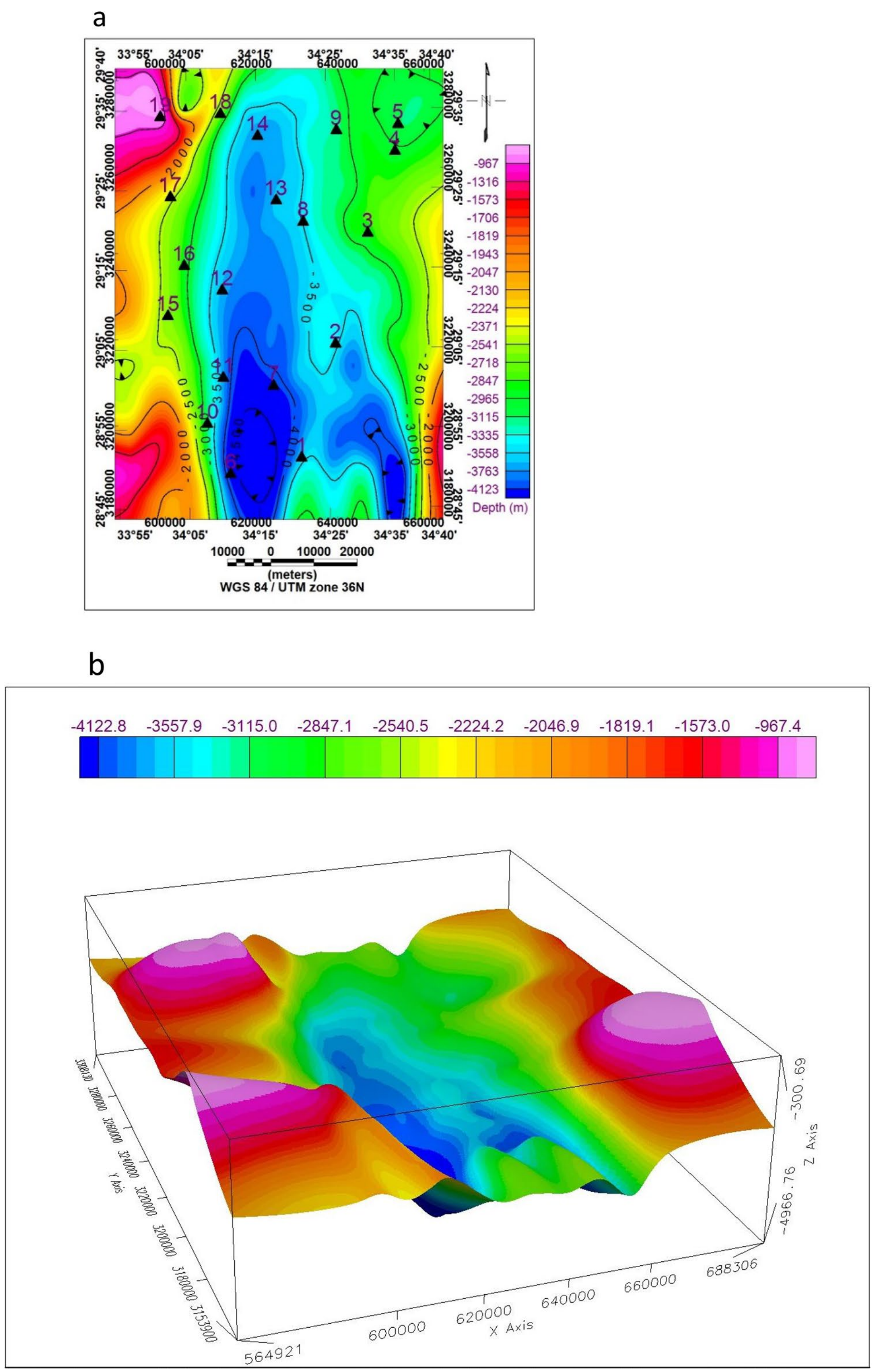

Fig. 8 **a** represents the basement relief map of the studied area, where **b** represents the 3D view for the top of basement surface

northwestern and northeastern parts have low resistivity values ranging from 30 to 210 Ω m. This layer comprises sand and sandstone belonging to the Lower Cretaceous age representing the NSA (Fig. 11).

Porosity map (sixth geological unit) The porosity percentage was explained by the relation between porosity and electrical conductivity. Archie formulated the following equation (Archie 1942):

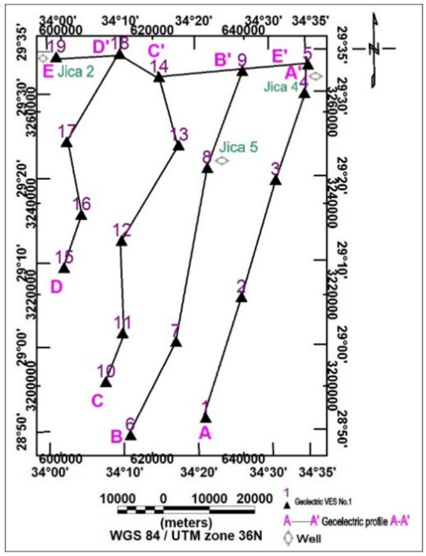

a Location of VES stations and geoelectric cross-sections, where the triangles represent the VES location and pink color represents the names of geoelectric cross-sections

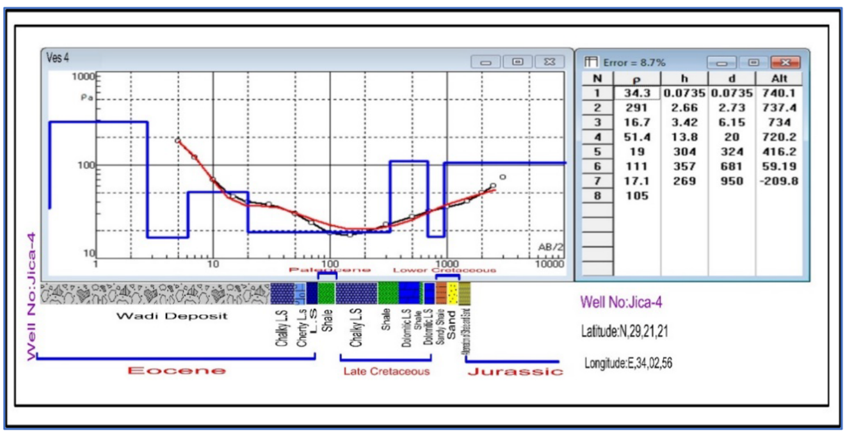

b Resistivity Models for VES 4 from the results of IPI2Win software and its correlation with the geological logs obtained from the Jica 4 boreholes map

Fig. 9 **a** Location of VES stations and geoelectric cross sections, where the triangles represent the VES location and pink color represents the names of geoelectric cross sections. **b** Resistivity models for VES 4 from the results of IPI2Win software and its correlation with the geological logs obtained from the JICA-4 boreholes map

$$\sigma_b = a\sigma_f \varphi^m$$

where σ_b and σ_f are the bulk and fluid, electrical conductivities, respectively; ɑ and m are constants for a rock of definite kind, and φ is the porosity. The aquifer in the investigated area comprises pure sandstone, as estimated from the results of the drilled borehole (JICA-4). Both ɑ and m are defined as per Senet al. 1988; Das et al. 2017, where ɑ = 1 and $m = 2$. The electric conductivity of the fluid, which is 0.1636 Siemens/m, is determined from the drilled borehole (JICA-4) in the central part of the investigated area. The results suggested that porosity had values of ~ 11–36%. The northeastern, southwestern, and eastern parts are determined by low porosity ranging from 11 to 12%, whereas the northwestern and eastern parts exhibit high porosity ranging from 24 to 36%. However, the central part is occupied by moderate porosity ranging from 12 to 24%; high porosity values are recorded at VES-17, whereas low porosity values are recorded at VES-7 (Fig. 11c).

Thickness map of NSA The depth of crystalline rocks can estimate NSA thickness from the magnetic interpretation and the depth of the top of NSA from the interpretation of geoelectrical data. The depth of the upper surface of the basement rocks represents the lower surface of NSA, where all rocks overlay the basement rocks represent the NSA. The

Fig. 10 One-dimensional geoelectric cross section along profiles: **a** ▸ P1; **b** P2; **c** P3; **d** P4; **e** P5

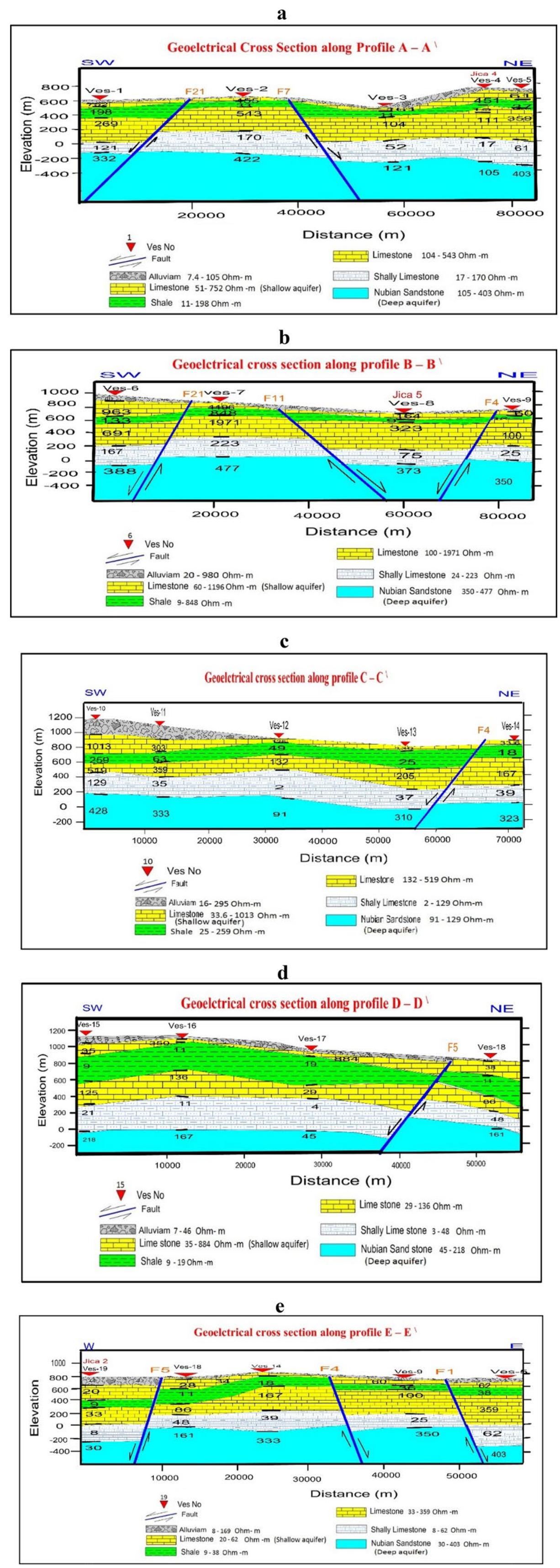

thickness map of NSA (Fig. 12a) demonstrates large thickness values at the southeastern and central parts of ~ 3000–3700 m, a thickness value of ~ 2000–3000 m in the northeastern and southern regions, and low thickness values at the western and northeastern parts (about ~ 1500–2000 m).

Priority map The priority map for the drilling plan is based on the interpretation of geophysical data. Figure 12b is divided into A, B, and C zones. A is the priority for the drilling plan, indicating low depth for the surface of the top of NSA, high thickness, and high resistivity values. These high resistivity values indicate good water quality (low salinity). The second and third priorities are B and C, respectively.

Discussion

The integrated geological boreholes and geophysical data confirm the results of the examined area where the results obtained from the interpretation of VES-19, VES-8, and VES-4 are compared with those of boreholes JICA-2, JICA-5, and JICA-4 (Fig. 1), indicating that results obtained from both VES and boreholes are compatible for the lithological successions, depth, and thickness of water-bearing zone (NSA) and water quality. Both borehole data and VES data interpretation indicated that the subsurface succession consists of six layers; the first layer comprises multiple rock fragments representing alluvial deposits with varying thicknesses of the Quaternary age. The second layer belongs to the Upper Cretaceous age and contains limestone of various thicknesses. The third geoelectrical unit includes a sandstone unit that belongs to the rocks of the Upper Cretaceous. The fourth layer comprises limestone and dolomitic limestone. The fifth layer comprises limestone, dolomite limestone, marls, and shales of the Upper Cretaceous. The sixth layer represents NSA in the examined area. The depth at the top of this unit is between 707 and 1154 m, which comprises thick-bedded grained sandstones, where the depth of groundwater aquifer (NSA) increases from the southeastern part to southwestern and western parts, then the flow of groundwater from southeast to the southwestern and west direction (Fig. 11a). Also, the recharge coming from the southeastern part of the area the age of this unit (aquifer) is the Lower Cretaceous which exhibits low salinity water in the investigated area. The resistivity values for groundwater aquifer are compatible with the salinity of borehole JICA-4 where both results show that the water quality is the freshwater of resistivity values for NSA ranging from 30.2 to 477 Ω m, as well as TDS recorded from the borehole of ~1047 ppm (Fig. 11b).

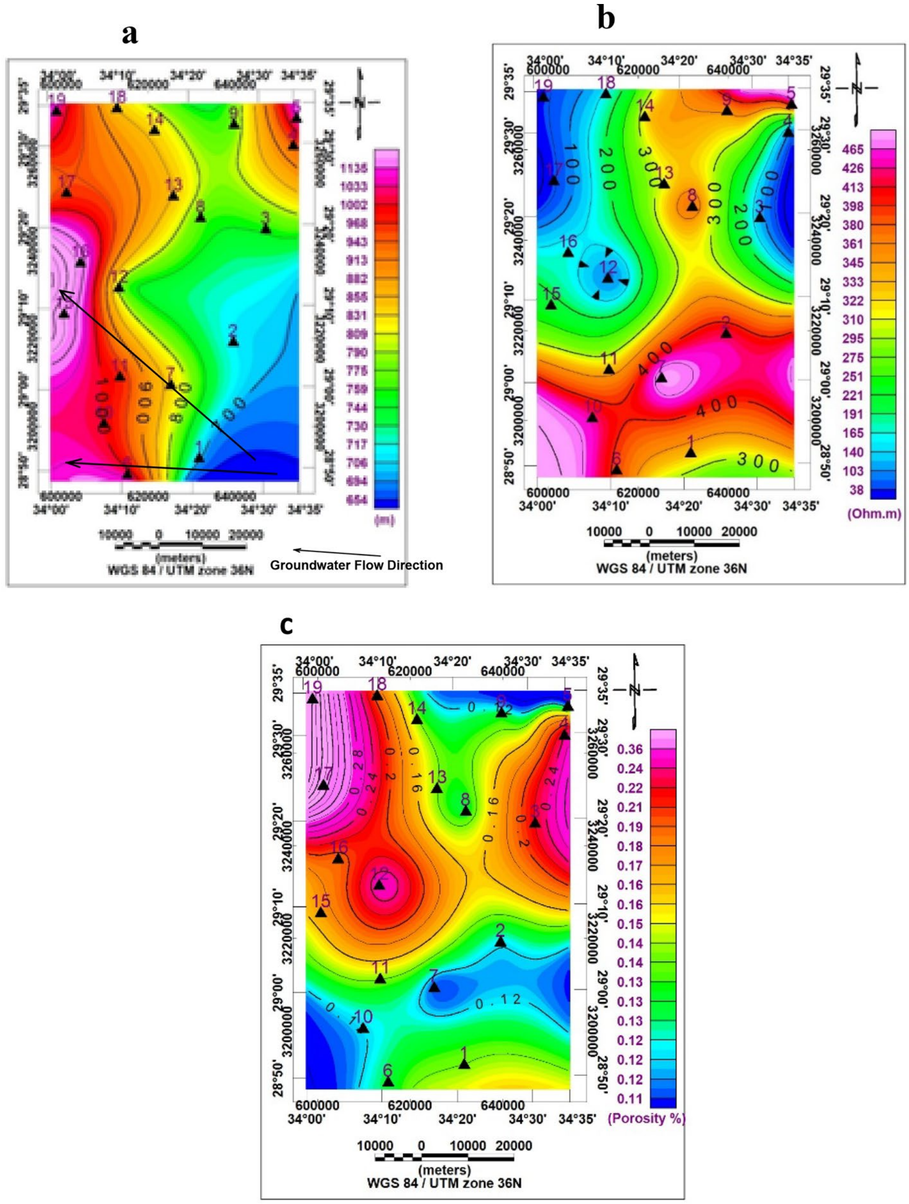

Fig. 11 **a** Depth map of Nubian sandstone aquifer; **b** isoresistivity map of Nubian sandstone aquifer; **c** porosity percentage of the studied area

The coupling of electrical resistivity, gravity, and magnetic techniques managed the structural conditions of the subsurface and assessment of the groundwater aquifer in the investigated area. Furthermore, the delineating fault elements derived from, the residual gravity anomaly map for the fourth-order, a high-pass filter map, and Euler deconvolution are all compatible (Fig. 5), where the main trend for most structural elements is NE-SW parallel to the Gulf of Aqaba. The investigated area is dissected by several fault elements, and these faults have been a direct effect on the distribution and hydraulic parameters of NSA. The large variation of hydraulic conductivity and transmissivity is due to structural features in the area.

Conclusion

From the results of drilled boreholes and geophysical data, the results obtained are as follows. The investigated area is determined using multiple structural features of northwest–southeast, northeast–southwest, and east–west trends; however, the important trend is [northeast–southwest (parallel to the Gulf of Aqaba direction)]. The subsurface sequence of the investigated area comprises six geoelectrical units composed of different lithological units belonging to different geological ages from the Lower Cretaceous to the Quaternary. The upper surface of the sixth geoelectrical unit (NSA) is delineated at depths varying

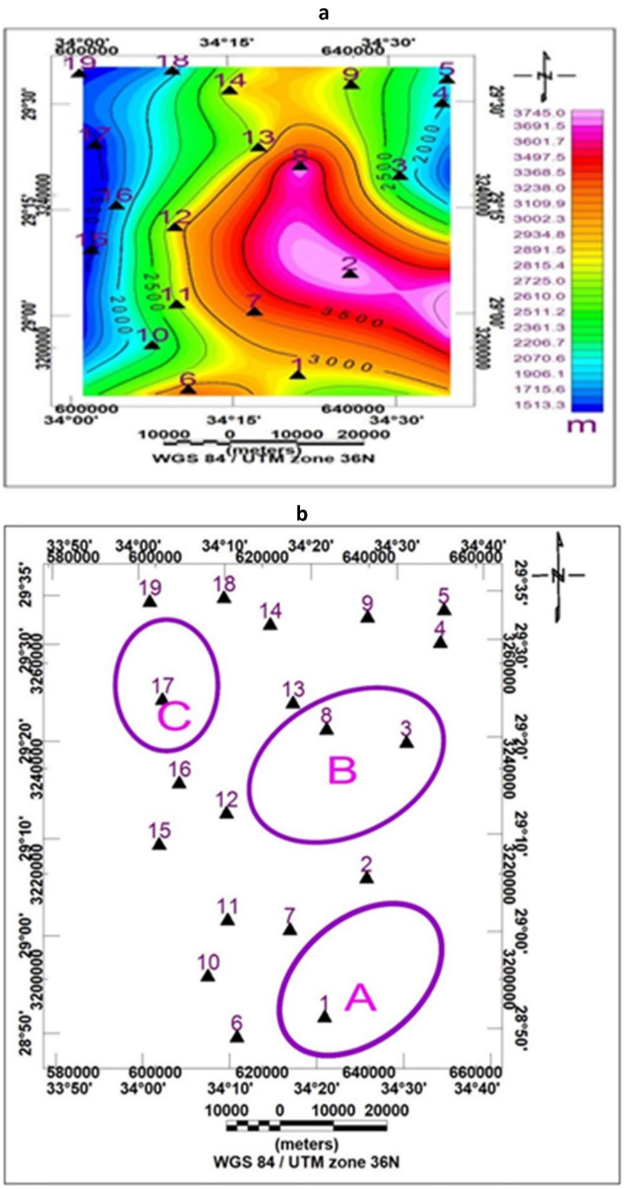

Fig. 12 **a** Isopach map of the Nubian sandstone, **b** priority map of the studied area, where **A** represents the first priority, **B** represents the second priority, **C** represents the third priority

from 707 to 1154 m; this unit is the primary aquifer in the investigated area characterized by freshwater quality as per the hydrochemistry of boreholes and resistivity values. The basement depth extends from 967 to 4122 m; the results suggest that the investigated area's southeastern part (zone A) is the best location for drilling, as reported in the priority map.

Acknowledgements The authors thank the teamwork of the National Research Institute of Astronomy and Geophysics (NRIAG) for helping in data collection.

Author contributions All authors shared in data collection, data interpretation, and preparation of the manuscript.

Funding Open access funding provided by The Science, Technology & Innovation Funding Authority (STDF) in cooperation with The Egyptian Knowledge Bank (EKB). This work was not funded.

Data availability The data that were collected for this work are available.

Code availability Not applicable.

Declarations

Conflict of interest The authors declare that they have no competing interests.

Ethical approval The authors approve for all states of this work.

Consent to participate All authors consent to participate.

References

Abdel ZM, Elbarbary S, Sultan SA, El-Qady G, Ismail A, Takla EM (2018) Crustal thermal structure of the Farafra oasis Egypt, based on airborne potential field data. GeothermicsVolume 75:220–234

Araffa SAS (2010) Geophysical investigation for shallow subsurface geotechnical problems of Mokattam area, Cairo, Egypt. Environ Earth Sci 5(6):1195–1207

Araffa SAS (2013) Delineation of under groundwater aquifer and subsurface structures in north Cairo, Egypt, used integrated interpretation of magnetic, gravity, and geoelectrical data. Geophys J Int 192(1):94–112

Araffa SAS, El Shayeb HM, Abu-Hashish MF, Hassan NM (2015) Integrated geophysical interpretation for delineating the structural elements under groundwater aquifers at the central part of Sinai Peninsula. Arab J Geosci 8(10):7993–8007. https://doi.org/10.1007/s12517-015-1824-5,8:7993-8007

Araffa SAS, El Nabi A, Sami H, Helaly AS, Dawoud MA, Sharkawy MS, Hassan NM (2022) Groundwater aquifer assessment using hydrogeophysical investigations: the case of western Al Ain Sokhna area Gulf of Suez, Eastern Desert, Egypt. Geocarto Int. https://doi.org/10.1080/10106049.2022.2109762

Archie GE (1942) The electrical resistivity log as an aid in determining some reservoir characteristics. Trans AIME 146:54–62

Baranov V (1957) A new method for interpretation of aeromagnetic maps: pseudo-gravimetric anomalies. Geophysics 22:359–383

Baranov V, Naudy H (1964) Numerical calculation of the formula of reduction to the magnetic pole. Geophysics 29:67–79

Baranov V (1975) Potential fields and their transformation in applied geophysics, *Geoexploration Monographs, series 1–6*, Gebrüder, Borntraeger, Berlin—Stuttgart

Bhattacharyya BK (1965) Two-dimensional harmonic analysis as a tool for magnetic interpretation. Geophysics 30(5):829–857

Binley A, Hubbard SS, Huisman JA, Revil A, Robinson DA, Singha K, Slater LD (2015) The emergence of hydro-geophysics for improved understanding of subsurface processes over multiple scales. Water Resour Res 51(6):3837–3866

Bobachev A, Modin I, Shevnin V (2001) IPI2Win software Geoscan-M Ltd. Moscow State University

Busch S, Weihermueller L, Huisman JA, Steelman CM, Endres AL, Vereecken H, der Kruk V (2013) Coupled hydrogeophysical inversion of time-lapse surface GPR data to estimate hydraulic properties of a layered subsurface. Water Resour Resour 49(12):8480–8494. https://doi.org/10.1002/2013WR013992

Camporese M, Cassiani G, Deiana R, Salandin P (2012) Assessment of local hydraulic properties from electrical resistivity tomography monitoring of a three-dimensional synthetic tracer test experiment. Water Resour Res 47:W12508. https://doi.org/10.1029/2011WR010528

Das A, Maiti S, Naidu S, Gupta G (2017) Estimation of spatial variability of aquifer parameters from geophysical methods: a case study of Sindhudurg district, Maharashtra, India. Stoch Environ Res Risk Assess 31:1709–1726. https://doi.org/10.1007/s00477-016-1317-4

Deep MA, Araffa SA, Mansour SA, Taha AI, Mohamed A, Othman A (2021) Geophysics and remote sensing applications for groundwater exploration in fractured basement: a case study from Abha area Saudi Arabia. J Afr Earth Sci 184:104368

Dlubac K, Knight R, Song YQ, Bachman N, Grau B, Cannia J, Williams J (2013) Use of NMR logging to obtain estimates of hydraulic conductivity in the High Plains aquifer, Nebraska, USA. Water Resour Res 49:1871–1886. https://doi.org/10.1002/wrcr.20151

El-Badrawy HT, Araffa SAS, Gabr AF (2021) Application of the multi-potential geophysical techniques for under groundwater evaluation in a part of Central Sinai Peninsula, Egypt. Acta Geodyn Geomater 18(201):61–70. https://doi.org/10.13168/AGG.2021.0004

El-Badrawy HT, Araffa SAS, Gabr Gabr AF (2021) Application of the multi potential geophysical techniques for groundwater evaluation in a part of central Sinai Peninsula, Egypt. Acta Geodyn Geomater 18(201):61–70

Elbarbary S, Araffa SAS, El-Shahat A, AbdelZaher M, Khedher KM (2021) Delineation of water potentiality areas at Wadi El-Arish, Sinai, Egypt, using hydrological and geophysical techniques. J Afr Earth Sc 174:104056

Feng W, Zhong MJ, Lemoine MR, Biancale H, Hsu T, Xia J (2013) Evaluation of under groundwater depletion in North China using the gravity recovery and climate experiment (GRACE) data and ground-based measurements. Water Resour Res 49:211–218. https://doi.org/10.1002/wrcr.20192

Gian PD, Ernesto B, Cristina M (2003) Inversion of electrical conductivity data with Tikhonov regularization approach: some considerations. Ann Geophys 46:3

Hassanin AM (1997) Geological and geomorphological impacts on the water resources in central Sinai, Egypt. Ph. D. Thesis, Geol. Dept., Fac. of Sci., Ain- Shams Univ., ARE, 373 p

Hinnell AC, Ferre TPA, Vrugt JA, Huisman JA, Moysey S, Rings J, Kowalsky MB (2010) Improved extraction of hydrologic information from geophysical data through coupled hydrogeophysical inversion. Water Resour Res 46:W00D40. https://doi.org/10.1029/2008WR007060

Ibrahim EH, Shereef MR, El Galladi AA, Pederson LB (2004) Geoelectric study on Quaternary under groundwater aquifer in northwestern Sinai. Egypt EGS J 2(1):69–74

Irving JD, Singha K (2010) Stochastic inversion of tracer test and electrical geophysical data to estimate hydraulic conductivities. Water Resour Res 46:W11514. https://doi.org/10.1029/2009WR008340

JICA (1992) North Sinai under groundwater resources study in the A. R. E: final report submitted to the Research Institute for Water Resources, Ministry of Public Works and Water Resources, Cairo, Egypt

Koefoed O (1960) A generalized Cagniard graph for interpretation of geoelectric sounding data. Geophys Prospect 8(3):459–469

Linde N, Doetsch J (2016) Joint inversion in hydrogeophysics and near-surface geophysics. In: Moorkamp M, Lelievre P, Linde N, Khan A (eds) Integrated imaging of the Earth, Chapter 7. Wiley, Hoboken, pp 119–135. https://doi.org/10.1002/9781118929063.ch7

Mohamed AME, Araffa SAS, Mahmoud NI (2012) Delineation of near-surface structure in the southern part of 15th of May City, Cairo, Egypt using geological, geophysical and geotechnical techniques. Pure Appl Geophys 169(9):1641–1654

Oasis Montaj (2015) Geosoft mapping and processing systems, geosoft Inc., suit500, Richmondst. West Toronto, ON Canada N5UIV6

Nabighian MN, Macnae JC (1991) Time-domain electromagnetic prospecting methods, In: Nabighian MN (Eds), Electromagnetic methods in applied geophysics, Society of Exploration Geophysics, Vol 2, pp 427–520

Parsekian AD, Singha K, Minsley BJ, Holbrook WS, Slater L (2015) Multiscale geophysical imaging of the critical zone. Rev Geophys 53(1):1–26

Pollock DW, Cirpka OA (2012) Fully coupled hydrogeophysical inversion of a laboratory salt tracer experiment monitored by electrical resistivity tomography. Water Resour Res 48:W01505. https://doi.org/10.1029/2011WR010779

Rubin Y, Hubbard SS (2006) Hydrogeophysics, vol 50. Springer, Berlin

Said R (1962) The geology of Egypt. Elsevier, Amsterdam

Santos FAM, Sultan SA, Patricia R, El Sorady AL (2006) Joint inversion of gravity and geoelectrical data for under groundwater and structural investigation: application to the northwestern part of Sinai. Egypt Geophys J Int 165:705–718

Sen PN, Goode PA, Sibbit A (1988) Electrical conduction in clay-bearing sandstones at low and high salinities. J Appl Phys 63:4832–4840

Shebl A, Abdelaziz MI, Ghazala H, Araffa SA, Abdellatif M, Csámer Á (2022) Multi-criteria groundwater potentiality mapping utilizing remote sensing and geophysical data: a case study within Sinai Peninsula Egypt. Egypt J Remote Sens Space Sci 25(3):765–778

Sultan SA, Santos FAM (2008) Evaluating subsurface structures and stratigraphic units using 2D electrical and magnetic data at the area north Greater Cairo, Egypt. Int J Appl Earth Observ Geoinform 10(1):56–67

Sultan SA, Mekhemer HM, Santos FAM, Abd AM (2009) Groundwater exploration and evaluation by using geophysical interpretation (case study: Al Qantara East, North Western Sinai, Egypt). Arab J Geosci 2:199–211

Telford WM, Geldart LP, Sheriff RE (1995) Applied geophysics. Cambridge University Press

Thorweihe U, Heinl M (2002) Groundwater resources of the Nubian Aquifer System, NE-Africa. Synthesis, Observatoire du Sahara et du Sahel, Paris

UNSECO Cairo Office (2005) Geologic Map of Sinai, Egypt, Scale 1:500, 000, Project for the Capacity Building of the Egyptian Geological survey and Mining Authority and the National Authority for

Remote Sensing and Space Science in Cooperation with UNDP and UNSECO. Geological Survey of Egypt

Van Dam RL, Eustice BP, Hyndman DW, Wood WW, Simmons CT (2014) Electrical imaging and fluid modeling of convective fingering in a shallow water-table aquifer. Water Resour Res 50:954–968. https://doi.org/10.1002/2013WR013673

Zohdy AR, Eaton G, Mabey D (1974) Application of surface geophysics to water investigations: techniques of water resources investigation of the United States Geological Survey, Book 2. Chapter D 1:116p